Evidence for a Fe^{3+}–rich pyrolitic lower mantle from (Al,Fe)–bearing bridgmanite elasticity data

A. Kurnosov[1], H. Marquardt[1], D. J. Frost[1], T. Boffa Ballaran[1] & L. Ziberna[1,2]

The chemical composition of Earth's lower mantle can be constrained by combining seismological observations with mineral physics elasticity measurements[1–3]. However, the lack of laboratory data for Earth's most abundant mineral, $(Mg,Fe,Al)(Si,Al,Fe)O_3$ bridgmanite (also known as silicate perovskite), has hampered any conclusive result. Here we report single-crystal elasticity data on (Al,Fe)-bearing bridgmanite $(Mg_{0.9}Fe_{0.1}Si_{0.9}Al_{0.1})O_3$ measured using high-pressure Brillouin spectroscopy and X-ray diffraction. Our measurements show that the elastic behaviour of (Al,Fe)-bearing bridgmanite is markedly different from the behaviour of the $MgSiO_3$ endmember[2,4]. We use our data to model seismic wave velocities in the top portion of the lower mantle, assuming a pyrolitic[5] mantle composition and accounting for depth-dependent changes in iron partitioning between bridgmanite and ferropericlase[6,7]. We find excellent agreement between our mineral physics predictions and the seismic Preliminary Reference Earth Model[8] down to at least 1,200 kilometres depth, indicating chemical homogeneity of the upper and shallow lower mantle. A high Fe^{3+}/Fe^{2+} ratio of about two in shallow-lower-mantle bridgmanite is required to match seismic data, implying the presence of metallic iron in an isochemical mantle. Our calculated velocities are in increasingly poor agreement with those of the lower mantle at depths greater than 1,200 kilometres, indicating either a change in bridgmanite cation ordering or a decrease in the ferric iron content of the lower mantle.

Quantitative knowledge of the chemistry, mineralogy and temperature of the lower mantle is of key importance for interpreting the thermal evolution, geochemical properties, and dynamics of Earth's interior. Pyrolite is a widely accepted model composition of Earth's upper mantle[5], which is broadly consistent with the composition of mantle rocks brought by volcanism to Earth's surface. It remains unclear, however, if pyrolite is also representative of the composition of the lower mantle or if the 660 km seismic discontinuity that marks the transition to the lower mantle is also a chemical boundary[2]. Direct constraints on the chemical and mineralogical composition of Earth's lower mantle can be derived through a comparison of seismic wave velocity models with synthetic mineral-physics-based velocity models calculated from laboratory elasticity measurements[1,2]. At lower mantle conditions, pyrolite composition rocks would be comprised of approximately 75 vol% of $(Mg,Fe,Al)(Si,Al,Fe)O_3$ bridgmanite, 18 vol% of $(Mg,Fe)O$ ferropericlase, and 7 vol% of $CaSiO_3$ perovskite[7].

On the basis of elasticity measurements on Al-bearing $MgSiO_3$, a recent study proposed that the lower mantle contains 93 vol% of bridgmanite[2], thereby supporting the hypothesis of a chemical boundary between the upper and lower mantle. In the absence of experimental data on the elastic properties of (Al,Fe)-bearing bridgmanite, this interpretation was based on the elastic properties of Al-bearing but Fe-free bridgmanite. In the lower mantle, however, an energetically favourable coupled substitution of Fe^{3+} (ferric iron) and Al^{3+} for Mg^{2+} and Si^{4+} leads to an increased Fe^{3+} content in

bridgmanite when Al^{3+} becomes available through the breakdown of majoritic garnet in the uppermost lower mantle[9]. The effect of coupled Fe^{3+} and Al^{3+} substitution on the elastic properties and seismic wave velocities of bridgmanite, which has remained unconstrained by experiments, is therefore critical to construct reliable seismic models. In contrast to the experimentally derived conclusion, computational studies that have attempted to predict the effects of Fe and Al incorporation on the bulk elastic properties of bridgmanite have proposed that a pyrolitic mantle may be consistent with seismic data[10,11]. Here we report simultaneous elastic wave velocity and density measurements on single crystals of $(Mg_{0.9}Fe_{0.1}Si_{0.9}Al_{0.1})O_3$ bridgmanite, a composition very close to that expected for bridgmanite in a pyrolitic mantle[7], to pressures of the lower mantle using a novel experimental approach (Fig. 1, see Methods). Single crystals of (Al,Fe)-bearing bridgmanite synthesized in a large-volume multi-anvil press were parallel-polished into disks and half-circle-shaped samples were cut using a focused ion beam[12]. Two half-circular samples with different crystallographic
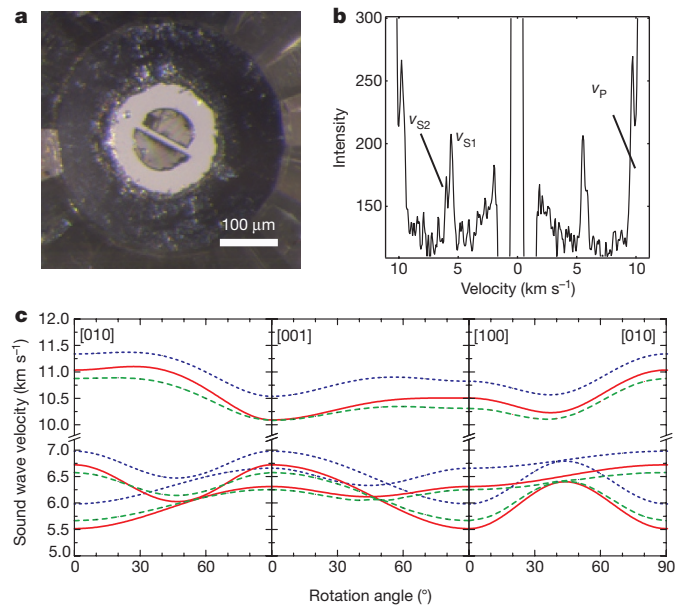

Figure 1 | Experimental setup and results. a, Two half-circular samples of single-crystal (Al,Fe)-bearing bridgmanite with different crystallographic orientations were loaded into the sample chamber of one diamond-anvil cell using helium as a pressure-transmitting medium. **b**, A Brillouin spectrum collected at 31.8 GPa is shown. Brillouin measurements were performed on both samples as a function of rotation angle. **c**, Velocity dispersion curves at ambient conditions calculated from our work (red solid curves) in comparison to previous experimental work on $MgSiO_3$ bridmanite[13] (blue dotted curves), as well as computational work on (Al,Fe)-bearing bridgmanite[14] (green dashed curves).

[1]Bayerisches Geoinstitut BGI, University of Bayreuth, 95440 Bayreuth, Germany. [2]University of Bristol, School of Earth Sciences, Bristol BS8 1RJ, UK.
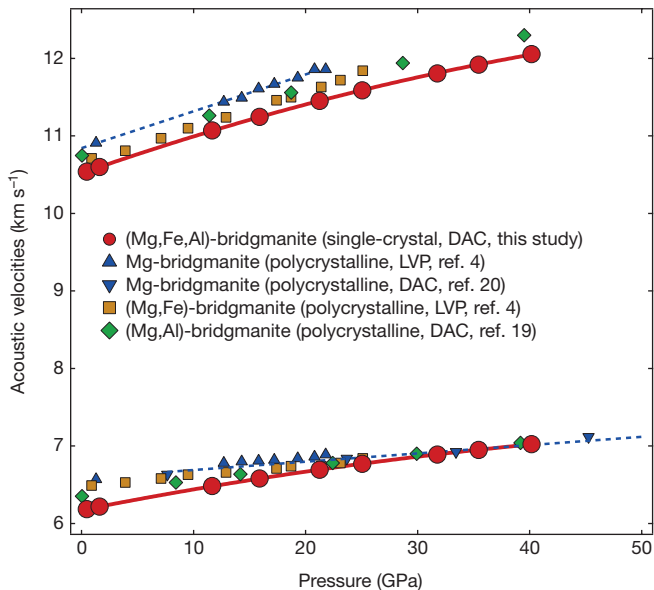
Figure 2 | Pressure dependence of the average acoustic velocities of (Al,Fe)-bearing bridgmanite (red circles). The uncertainties in acoustic velocities are smaller than the symbol size. Previously published measurements on polycrystalline bridgmanite with different chemical compositions are shown for comparison (refs 2, 4, 13, 15, 16, 19, 20). The blue dotted line indicates the pressure-trend of Mg-endmember bridgmanite: incorporation of Al and Fe reduces the acoustic velocities at room pressure, but the stronger pressure dependence of the shear velocities leads to a shear velocity crossover with MgSiO$_3$ bridgmanite at pressures above approximately 35 GPa. DAC, diamond-anvil cell; LVP, large-volume press.

orientations were loaded into the sample chamber of one diamond-anvil cell. High-pressure elasticity and density measurements were performed using a combined Brillouin scattering and X-ray diffraction system at the Bayerisches Geoinstitut (Extended Data Table 1).

A global fit of a third-order Eulerian finite strain equation to all our high-pressure data yields the following best-fit elastic constants, C_{ij}, at room pressure, where the number in brackets refers to the 1σ uncertainty in the last given digit: $C_{11} = 461.3(17)$ GPa; $C_{22} = 509.7(26)$ GPa; $C_{33} = 425.7(5)$ GPa; $C_{44} = 188.8(6)$ GPa; $C_{55} = 166.5(4)$ GPa; $C_{66} = 127.2(17)$ GPa; $C_{12} = 141.7(14)$ GPa; $C_{13} = 130.0(11)$ GPa; $C_{23} = 161.0(12)$ GPa. Figure 1c shows a comparison of the velocity dispersion in (Al,Fe)-bearing bridgmanite derived from this study to
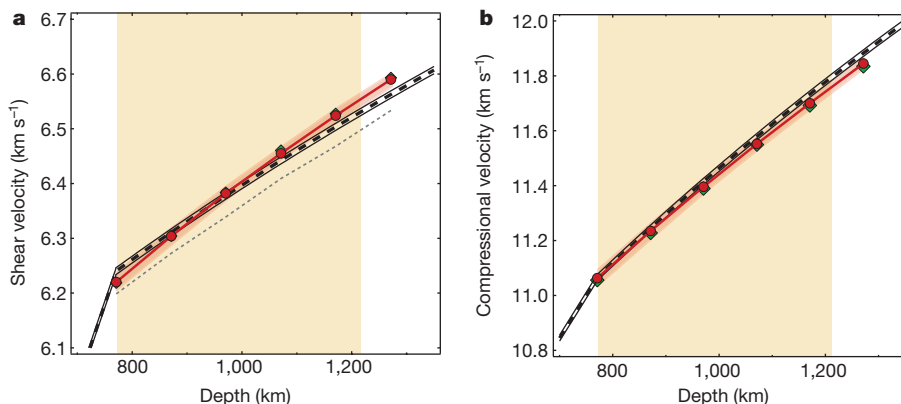
pure MgSiO$_3$ bridgmanite[13], as well as computational results[14]. There is generally good agreement between our measured elastic constants for (Mg$_{0.9}$Fe$_{0.1}$Si$_{0.9}$Al$_{0.1}$)O$_3$ and those predicted by computations for (Mg$_{0.9375}$Fe$_{0.0625}$Si$_{0.9375}$Al$_{0.0625}$)O$_3$ (ref. 14), as shown in Extended Data Table 2.

From our global fit, we derive the adiabatic bulk K_s and shear modulus G, as well as their pressure derivatives $K'_{s,0}$ and G'_0, as follows: $K_{s,0} = 250.8(4)$ GPa, $K'_{s,0} = 3.44(3)$, $G_0 = 159.7(2)$ GPa, $G'_0 = 2.05(2)$. Comparison of our direct elasticity measurements to previous results on MgSiO$_3$ using Brillouin scattering[13,15] and ultrasonics[4,16] confirms that coupled substitution of Al and Fe lowers the bulk modulus, as suggested on the basis of high-pressure single-crystal X-ray diffraction (XRD) experiments[17] and computational work[14,18]. Our data show that coupled substitution of Al and Fe also lowers the shear modulus, which is similar to the effect observed for Al-incorporation alone[2,19]. This experimental finding is consistent with computational results[14,18] (Extended Data Fig. 1). The fit to our data, however, requires a substantially larger pressure derivative of the shear modulus, as compared to pure MgSiO$_3$ ($G'_0 = 1.6$) (refs 4, 20), Al-bearing bridgmanite containing 4–5 wt% Al$_2$O$_3$ ($G'_0 = 1.6$–1.7) (refs 2, 19), or bridgmanite containing mostly ferrous iron (Mg$_{0.95}$Fe$_{0.05}$SiO$_3$; $G'_0 = 1.6$) (ref. 4). This observation points to a unique effect that coupled Al^{3+} and Fe^{3+} substitution has on the shear elasticity of bridgmanite. We note that the pronounced increase of the derivative of the shear modulus is not captured by previous computational studies that report only very minor changes of G'_0 caused by the addition of the FeAlO$_3$ component to MgSiO$_3$ bridgmanite[10,18].

From the derived elastic moduli and the measured densities, we calculated the average compressional and shear wave velocities of (Al,Fe)-bearing bridgmanite (Fig. 2). Our results show that incorporation of Al and Fe reduces the acoustic velocities at room pressure, but the stronger pressure dependence of the shear modulus leads to a shear velocity crossover with MgSiO$_3$ bridgmanite at pressures of the lower mantle (Fig. 2).

We use our elasticity results to model one-dimensional seismic wave velocity profiles for the uppermost lower mantle (Fig. 3, Extended Data Fig. 2). For the models, we refine elastic properties for the bridgmanite (as well as ferropericlase) solid solution components based on our data and combine these with thermodynamic determinations of the Fe–Mg partitioning between bridgmanite and ferropericlase to determine mineral compositions and seismic velocities with depth (see Extended Data Figs 3–5). We did not include the upper approximately 100 km of the lower mantle in our model as seismic wave speeds at these depths are influenced by the breakdown of majoritic garnet, which adds uncertainties to the modelling. Similarly, we did not extrapolate our model

Figure 3 | Mineral-physics-based seismic models. a, b, Comparison of calculated seismic shear (**a**) and compressional (**b**) velocities in the shallow lower mantle to PREM. Full symbols: models that have been calculated assuming Fe^{2+} disproportionation (red) and assuming no disproportionation (green). The shaded region illustrates the Voigt–Reuss

bounds for the red model. The thick dashed line shows the PREM along with a 0.2% uncertainty (thin lines). The yellow-coloured area indicates the depth region where our pyrolitic seismic model agrees with the PREM within the Voigt–Reuss bounds. The grey dotted line shows the results of our model when neglecting the FeAlO$_3$ component of bridgmanite.
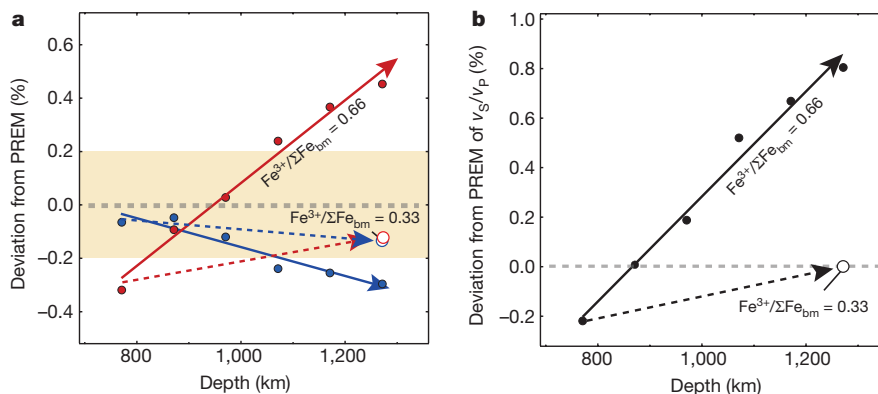
Figure 4 | Deviation of modelled seismic velocities from PREM with depth. a, Deviation of shear (red) and compressional velocities (blue) from PREM. The dashed region indicates 0.2% uncertainty in seismic velocities. **b**, Deviation of the ratio of S-wave to P-wave velocity (v_S/v_P) from PREM.

The solid lines indicate the model results with the assumption of constant ferric iron content in bridgmanite. The dashed lines show results from the same model, but under the assumption that the ferric iron content in bridgmanite decreases with depth. bm, bridgmanite.

beyond a depth of 1,350 km as the effects of the iron spin crossover in ferropericlase, and possibly in bridgmanite, on the iron partitioning behaviour and the elastic properties are not sufficiently quantified[1,21].

We calculated two possible seismic profiles on the basis of different assumptions concerning the oxygen distribution in the mantle. This is motivated by previous experimental findings showing that Al-bearing bridgmanite always contains a large proportion of Fe^{3+}, regardless of the redox conditions of the experiments[22,23], implying that the lower mantle contains significantly more ferric iron than the upper mantle. This observation allows for two possible scenarios[22], in which (1) the bulk oxygen content of the lower mantle is higher than that of the upper mantle, or (2) the bulk oxygen content remains constant throughout the mantle, resulting in metallic iron formation in the lower mantle owing to disproportionation of $Fe^{2+}O$ to form metallic Fe and $Fe_2^{3+}O_3$ (ref. 22). In both models, we constrained the $Fe^{3+}/\Sigma Fe$ fraction in bridgmanite to a value of 0.66, consistent with the results of previous experiments carried out at shallow-lower-mantle conditions[7]. We find that both of our models agree with the Preliminary Reference Earth Model (PREM)[8] to a depth of approximately 1,200 km within 0.2%, that is, within the range of expected uncertainties in seismic velocities in the lower mantle[3]. Our calculations therefore show that pyrolite is an excellent average model composition for the shallow lower mantle that can thus be considered isochemical to the upper mantle. This finding is consistent with geophysical observations that show slabs to enter the lower mantle[24], geodynamic simulations that favour whole mantle convection styles[25], and petrological findings of lower mantle inclusions in diamonds found on the surface of Earth[26]. Our measured low value of the pressure derivative of the bulk modulus $K'_{s,0}$ confirms a previous prediction that $K'_{s,0}$ for bridgmanite would have to be less than 4 for PREM velocities to be consistent with a pyrolitic mantle model[27].

The agreement of our disproportionation model to PREM also indirectly supports a constant oxygen content in the mantle and the presence of a small amount of metallic iron, as expected for a truly isochemical mantle[22]. This finding is supported by the occurrence of iron metal inclusions in some sublithospheric diamonds[28]. We note that the pressure range of our model is almost entirely covered by our experimental data on bridgmanite, as well as available data for $(Mg_{0.9}Fe_{0.1})O$ ferropericlase[29], with almost the same chemical composition as expected in a pyrolitic mantle. Therefore, no significant extrapolations in pressure or composition are required (Extended Data Figs 3, 4). The thermal parameters for the $MgSiO_3$ component are well-constrained by recent experiments[2,4] and computations[30], and a recent computational study indicates only minor effects of the $FeAlO_3$ component on thermal elastic properties compared to $MgSiO_3$ (ref. 18). A model in which all Fe and Al in bridgmanite is assumed to be accommodated by the $FeSiO_3$ and $AlAlO_3$ components provides a poorer fit to PREM velocities (Fig. 3a).

Despite the match of the absolute velocities found in our model to seismic data, our mineral physics models indicate a systematically increasing deviation of both compressional and shear wave velocities from PREM with depth (Figs 3, 4). This implies that the velocity gradients derived from seismology, which are tightly constrained by observations[1,3], are not fully captured by our model. It is important to note that our modelled shear and compressional velocities deviate from PREM in opposite directions. Therefore, the systematic difference between our model and PREM cannot be reconciled by employing a sub- or superadiabatic geotherm or by changing the major chemistry of the mantle with depth. Even though some uncertainties remain regarding the quantitative effects of the Fe^{2+} spin crossover in ferropericlase on seismic wave velocities, it is likely that the change of spin state will further increase the systematic difference between our model and PREM as it causes a significant reduction in compressional wave velocities in ferropericlase with depth but only slightly affects shear wave velocities[21,29]. At greater depths, the site ordering of Al and Fe in bridgmanite might change[31]. Such a process could affect seismic velocities, but quantitative predictions are difficult to perform. We find, however, that the velocity differences between our model and PREM can be minimized by allowing for a depth-dependent change of the ferric iron content in bridgmanite (Fig. 4). According to our calculations, a decrease of $Fe^{3+}/\Sigma Fe$ in bridgmanite from 0.66 at around 800 km depth to about 0.33 at a depth of around 1,300 km results in velocity gradients of both shear and compressional velocities that match those of PREM within its uncertainties (Fig. 4). Such a possible decrease of ferric iron content in bridgmanite with depth would affect transport properties in the mantle, such as the electrical conductivity[32] and possibly mantle viscosity[33]. However, further work at higher pressures would be required to test these predictions.

1. Cammarano, F., Marquardt, H., Speziale, S. & Tackley, P. J. Role of iron-spin transition in ferropericlase on seismic interpretation: a broad thermochemical transition in the mid mantle? *Geophys. Res. Lett.* **37,** L03308 (2010).
2. Murakami, M., Ohishi, Y., Hirao, N. & Hirose, K. A perovskitic lower mantle inferred from high-pressure, high-temperature sound velocity data. *Nature* **485,** 90–94 (2012).
3. Cobden, L. *et al.* Thermochemical interpretation of 1-D seismic data for the lower mantle: the significance of nonadiabatic thermal gradients and compositional heterogeneity. *J. Geophys. Res.* **114,** B11309 (2009).
4. Chantel, J., Frost, D. J., McCammon, C. A., Jing, Z. & Wang, Y. Acoustic velocities of pure and iron-bearing magnesium silicate perovskite measured to 25 GPa and 1200 K. *Geophys. Res. Lett.* **39,** L19307 (2012).
5. Ringwood, A. E. A model for the upper mantle. *J. Geophys. Res.* **67,** 857–867 (1962).

6. Nakajima, Y., Frost, D. J. & Rubie, D. C. Ferrous iron partitioning between magnesium silicate perovskite and ferropericlase and the composition of perovskite in the Earth's lower mantle. *J. Geophys. Res.* **117,** B08201 (2012).
7. Irifune, T. *et al.* Iron partitioning and density changes of pyrolite in Earth's lower mantle. *Science* **327,** 193–195 (2010).
8. Dziewonski, A. M. & Anderson, D. L. Preliminary reference Earth model. *Phys. Earth Planet. Inter.* **25,** 297–356 (1981).
9. McCammon, C. Perovskite as a possible sink for ferric iron in the lower mantle. *Nature* **387,** 694–696 (1997).
10. Wang, X., Tsuchiya, T. & Hase, A. Computational support for a pyrolitic lower mantle containing ferric iron. *Nat. Geosci.* **8,** 556–559 (2015).
11. Zhang, S., Cottaar, S., Liu, T., Stackhouse, S. & Militzer, B. High-pressure, temperature elasticity of Fe- and Al-bearing $MgSiO_3$: implications for the Earth's lower mantle. *Earth Planet. Sci. Lett.* **434,** 264–273 (2016).
12. Marquardt, H. & Marquardt, K. Focused Ion Beam preparation and characterization of single-crystal samples for high-pressure experiments in the diamond-anvil cell. *Am. Mineral.* **97,** 299–304 (2012).
13. Sinogeikin, S. V., Zhang, J. & Bass, J. D. Elasticity of single crystal and polycrystalline $MgSiO_3$ perovskite by Brillouin spectroscopy. *Geophys. Res. Lett.* **31,** L06620 (2004).
14. Li, L. *et al.* Elasticity of (Mg, Fe)(Si, Al)O_3-perovskite at high pressure. *Earth Planet. Sci. Lett.* **240,** 529–536 (2005).
15. Yeganeh-Haeri, A. Synthesis and re-investigation of the elastic properties of single-crystal magnesium silicate perovskite. *Phys. Earth Planet. Inter.* **87,** 111–121 (1994).
16. Li, B. & Zhang, J. Pressure and temperature dependence of elastic wave velocity of $MgSiO_3$ perovskite and the composition of the lower mantle. *Phys. Earth Planet. Inter.* **151,** 143–154 (2005).
17. Boffa Ballaran, T. *et al.* Effect of chemistry on the compressibility of silicate perovskite in the lower mantle. *Earth Planet. Sci. Lett.* **333–334,** 181–190 (2012).
18. Shukla, G., Cococcioni, M. & Wentzcovitch, R. M. Thermoelasticity of Fe3+- and Al-bearing bridgmanite: effects of iron spin crossover. *Geophys. Res. Lett.* **43,** 5661–5670 (2016).
19. Jackson, J. M., Zhang, J., Shu, J., Sinogeikin, S. V. & Bass, J. D. High-pressure sound velocities and elasticity of aluminous $MgSiO_3$ perovskite to 45 GPa: implications for lateral heterogeneity in Earth's lower mantle. *Geophys. Res. Lett.* **32,** L21305 (2005).
20. Murakami, M., Sinogeikin, S. V., Hellwig, H., Bass, J. D. & Li, J. Sound velocity of $MgSiO_3$ perovskite to Mbar pressure. *Earth Planet. Sci. Lett.* **256,** 47–54 (2007).
21. Lin, J.-F., Speziale, S., Mao, Z. & Marquardt, H. Effects of the electronic spin transitions of iron in lower-mantle minerals: implications to deep-mantle geophysics and geochemistry. *Rev. Geophys.* **51,** 244–275 (2013).
22. Frost, D. J. *et al.* Experimental evidence for the existence of iron-rich metal in the Earth's lower mantle. *Nature* **428,** 409–412 (2004).
23. Sinmyo, R., Hirose, K., Muto, S., Ohishi, Y. & Yasuhara, A. The valence state and partitioning of iron in the Earth's lowermost mantle. *J. Geophys. Res.* **116,** B07205 (2011).
24. Fukao, Y. & Obayashi, M. Subducted slabs stagnant above, penetrating through, and trapped below the 660 km discontinuity. *J. Geophys. Res.* **118,** 2013JB010466 (2013).
25. Tackley, P. J. Mantle convection and plate tectonics: toward an integrated physical and chemical theory. *Science* **288,** 2002–2007 (2000).
26. Walter, M. J. *et al.* Deep mantle cycling of oceanic crust: evidence from diamonds and their mineral inclusions. *Science* **334,** 54–57 (2011).
27. Jackson, I. Elasticity, composition and temperature of the Earth's lower mantle: a reappraisal. *Geophys. J. Int.* **134,** 291–311 (1998).
28. Smith, E. M. *et al.* Large gem diamonds from metallic liquid in Earth's deep mantle. *Science* **354,** 1403–1405 (2016).
29. Marquardt, H., Speziale, S., Reichmann, H. J., Frost, D. J. & Schilling, F. R. Single-crystal elasticity of (Mg$_{0.9}$Fe$_{0.1}$)O to 81 GPa. *Earth Planet. Sci. Lett.* **287,** 345–352 (2009).
30. Zhang, Z., Stixrude, L. & Brodholt, J. Elastic properties of $MgSiO_3$-perovskite under lower mantle conditions and the composition of the deep Earth. *Earth Planet. Sci. Lett.* **379,** 1–12 (2013).
31. Catalli, K. *et al.* Effects of the Fe^{3+} spin transition on the properties of aluminous perovskite—new insights for lower-mantle seismic heterogeneities. *Earth Planet. Sci. Lett.* **310,** 293–302 (2011).
32. Xu, Y. & McCammon, C. Evidence for ionic conductivity in lower mantle (Mg,Fe)(Si,Al)O_3 perovskite. *J. Geophys. Res.* **107,** 2251 (2002).
33. Rudolph, M. L., Lekić, V. & Lithgow-Bertelloni, C. Viscosity jump in Earth's mid-mantle. *Science* **350,** 1349–1352 (2015).

Author Contributions A.K., H.M., D.F. and T.B.B. designed the research. L.Z. synthesized the bridgmanite sample. A.K. performed the experiments and analysed the Brillouin data. T.B.B. performed the XRD analysis. D.F. and H.M. discussed the content of the paper and performed the modelling. H.M. wrote the paper draft. All authors commented on the manuscript.

METHODS

Sample material. *Sample synthesis.* Large crystals (up to 150 μm in one dimension) of (Fe,Al)-bearing MgSiO₃ bridgmanite were grown from a mixture of high-purity oxides ($SiO_2 = 47.67$ wt%, $Mg(OH)_2 = 41.40$ wt%, $Al_2O_3 = 4.26$ wt%, $Fe_2O_3 = 6.67$ wt%). The starting material was ground in acetone for one hour and dried at 120 °C for 12 h. The multi-anvil experiment was performed using Cr_2O_3-doped MgO octahedra of 7 mm edge length in combination with tungsten carbide cubes with 3 mm truncation edge lengths. The cell assembly in the octahedron consisted of a $LaCrO_3$ heater, containing the starting material loaded in a gold capsule (diameter = 1 mm), and MgO sleeves and spacers isolating the capsule from the heater. The experiment was performed at 25 GPa. A step-heating procedure was adopted, in which temperature was estimated from the electrical power on the basis of previous calibrations that used type D thermocouples. The temperature was increased from 25 °C to approximately 1,400 °C in 30 min, kept constant for 5 min, then decreased to about 1,250 °C, kept constant for 15 min, and then quenched.

Sample characterization. Electron microprobe analysis of several crystals from the run product resulted in the following average composition: $SiO_2 = 52.56$ wt%, $MgO = 35.84$ wt%, $FeO = 7.18$ wt%, $Al_2O_3 = 4.42$ wt%. The calculated mineral formula is $Mg_{0.912(6)}Fe_{0.102(6)}Al_{0.089(7)}Si_{0.897(6)}O_3$. Within the uncertainties of the chemical analysis, the composition can be simplified to $Mg_{0.9}Fe_{0.1}Al_{0.1}Si_{0.9}O_3$, that is, a mixture of 90 mol% of MgSiO₃ component and 10 mol% of $AlFeO_3$ component. Fourier transform infrared spectroscopy did not indicate structurally incorporated OH.

Sample preparation. Selected single-crystals for bridgmanite were double-side polished to a thickness of about 10–15 μm. A FEI Scios focused ion beam machine was used to cut half-circles from the pre-polished single-crystal samples (Extended Data Fig. 6) for loading into the diamond-anvil cell[12,34,35]. Ion beam cutting was performed using an ion beam current of 15 nA at an acceleration voltage of 30 kV.

Brillouin and XRD measurements at high pressures. Two sample slices with different crystallographic orientations were loaded together with a ruby sphere in the pressure chamber of a single BX90-type diamond-anvil cell[36]. The diamond-anvil cell was equipped with Boehler-Almax-type diamonds (culets of 400 μm) and seats with 90° optical opening angles. Helium was used as pressure-transmitting medium and loaded at a pressure of 1.5 kbar using the gas-loading system at BGI Bayreuth[37].

Elastic wave velocities were measured using the Brillouin system at BGI Bayreuth, employing 532 nm laser light, a multi-pass tandem Fabry–Pérot interferometer and either a photomultiplier or avalanche photodiode for signal detection. Measurements were performed in symmetric forward scattering geometry[38] using a scattering angle of 80°. The sample was rotated around the compression direction of the diamond-anvil cell and Brillouin measurements were taken on each crystal at intervals of 5°–15° over an angular range of usually 360°. The typical signal collection time at high pressures was one to several hours. Signal from both the shear waves and the compressional waves could be collected at all experimental pressures, even though overlap between the compressional wave of the sample and the diamond shear wave started to occur at the highest pressures in certain directions. In ideal symmetric platelet scattering geometry, the acoustic wave velocities measured 180° from each other should be identical. However, a slight deviation from the ideal scattering geometry (inclination of sample plane, non-parallel diamond anvils, non-perfect sample polishing) may affect velocities[39,40] and lead to slight mismatches between velocities measured after 180° rotation. To quantify and correct for such deviations in our experiment, we measured sound wave velocities over the entire range of 360° with a typical step size of 10°. We detected small differences in velocities measured on one of the crystals after 180° rotation, whereas no difference was observed for the other. The large rotational range of data coverage and the small angular step size allowed for correction of this systematic mismatch by adding an angle-dependent sinus function in the fitting procedure used to extract the elastic constants from the measured velocities.

X-ray diffraction experiments were carried out on a Huber four-circle diffractometer with rotating anode X-ray source, multilayer focusing optics and a scintillation single-counter detector system. More details about the system can be found elsewhere[41]. The eight-position centring method implemented in the code SINGLE[42] was used for elimination of diffractometer aberration and crystal offsets. The unit cell volumes were determined from both crystals before and after the Brillouin measurements at each pressure step.

Data reduction. In symmetric platelet forward scattering geometry, the measured Brillouin frequency shifts $\Delta\omega$ are directly related to the acoustic velocities v through the identity[40]: $v = \Delta\omega\lambda/[2\sin(\theta/2)]$, with θ being the external scattering angle. The frequency to velocity conversion of the Brillouin spectra was regularly checked using a glass standard. Brillouin spectra measured in DAC very often have low photon count rate as the samples are thin and the diamond anvils contribute to the noise level. To apply an appropriate weighting scheme to our measurements

that takes into account the signal-to-noise ratio, we performed statistical analyses of our data. For this purpose, numerous peaks with different signal-to-noise ratios (from very bad to very good) were measured more than 20 times each and the standard deviation (s.d.), which represents the dispersion of individual (single) measurements around the mean value, was calculated (Extended Data Fig. 7; see also ref. 43). The data were interpolated with an exponential decay function as shown in Extended Data Fig. 7. On the basis of this dependency, we weighted all of our observed peaks with a weighting factor of $1/s.d.^2$ (instrumental weighting) to achieve a realistic contribution of every data point to the fitting procedure.

Values and uncertainties of the elastic constants C_{ij} and their pressure derivatives at ambient pressure were derived using a global fit of all our experimental data, combining the usually employed Christoffel equation that relates elastic constants and density to direction-dependent acoustic wave velocities[40] with the finite strain formalism (equation (31) in ref. 44). Input data for this fit were the experimentally measured acoustic velocities (about 100–150 individual velocities for each pressure point, with uncertainties as described above), the crystallographic orientation of the two sample platelets determined by *in situ* X-ray measurement, and the density determined from the X-ray unit cell volume for every pressure point. From these data, $C_{ij}(P)$, K_{Reuss}, K_{Voigt}, G_{Reuss} and G_{Voigt} were calculated at every experimental pressure (density) point and K_0, K'_0, G_0 and G'_0 were fit using finite strain equations.

The application of this global fitting scheme—which is only possible because we can measure the sample density at high pressure—significantly reduces the uncertainties in the ambient pressure values (due to high data redundancy). For comparison, we also fitted our data using the standard approach, in which every pressure point is first fitted individually using the Christoffel equation, and a finite strain equation is then applied in a second separate step. Using this approach, we derived the following parameters for the elastic moduli and their pressure derivatives: $K_{S,0} = 248.7(31)$ GPa, $K'_{S,0} = 3.43(21)$, $G_0 = 160.8(15)$ GPa, $G'_0 = 2.20(9)$, that is, within uncertainties these values agree with the ones obtained from the global fit, but have larger errors.

Modelling of phase equilibria and element partitioning. A bulk mantle composition[45] was assumed for modelling seismic wave velocities, where the oxide weight percentages have been fixed to a bulk silicate earth composition, normalized to five major oxides ($SiO_2 = 45.52$ wt%, $Al_2O_3 = 4.51$ wt%, $FeO = 8.14$ wt%, $MgO = 38.23$ wt%, $CaO = 3.59$ wt%).

Our model assumes that the lower mantle is composed of the phases bridgmanite, ferropericlase, Ca-perovskite, and metallic iron (in the disproportionation model only). Calculations were performed at pressures above 28 GPa, at which the lower mantle assemblage no longer contains garnet. The phases bridgmanite, as well as ferropericlase, are described by the endmember components MgSiO₃, $Fe^{2+}SiO_3$, $Fe^{3+}AlO_3$, $AlAlO_3$ in the case of bridgmanite and MgO and $Fe^{2+}O$ in the case of ferropericlase. The distribution of elements among the different phases and the relative contribution of the respective components are refined through a mass balance calculation that employs the following constraints. (1) CaSiO₃ perovskite is the only Ca-bearing phase and bridgmanite is the only Al-bearing phase. (2) The Fe^{2+}–Mg exchange coefficient between bridgmanite (bm) and ferropericlase (fper) K_D is defined as

$$K_D = \frac{X_{FeSiO_3}^{bm} X_{MgO}^{fper}}{X_{MgSiO_3}^{bm} X_{FeO}^{fper}}$$

where, for example, $X_{FeSiO_3}^{bm} = \frac{Fe^{2+}}{Fe^{2+} + Mg}$. K_D is calculated from the expression

$$RT\ln K_D = -\Delta G^0 + W_{FeMg}^{bm}(2X_{Fe}^{bm} - 1) + W_{FeMg}^{fper}(1 - 2X_{Fe}^{fper})$$

where R is the gas constant, W_{FeMg}^{bdg} and W_{FeMg}^{fper} are Margules interaction parameters for bridgmanite and ferropericlase that describe non-ideal Fe and Mg mixing and ΔG^0 is the standard state Gibbs free energy of the Fe–Mg exchange reaction[6]. ΔG^0 is calculated through a self-consistent thermodynamic formalism[46], employing the parameters in Extended Data Table 3. The equation of state parameters used for this calculation are, therefore, the same as those used for the calculation of the seismic model described below (Extended Data Table 3). Margules parameters $W_{FeMg}^{fper} = 11,000 + 110P$ J mol⁻¹, where P is pressure in GPa, and $W_{FeMg}^{bm} = 0$ J mol⁻¹, were determined by fitting experimental Fe–Mg partitioning data[6]. The calculated K_D values show a pressure trend in agreement with experimental data obtained on Al-free systems[6,7]. (3) The $Fe^{3+}/\Sigma Fe$ ratio in bridgmanite was fixed to 0.66 in agreement with multi-anvil experiments carried out at conditions corresponding to the top of the lower mantle[7]. The Fe^{3+} content of bridgmanite was then fixed by the Fe^{2+} content determined through constraint (2) combined with the mass balance. The apparent Fe–Mg exchange coefficient $K_{D(app)}$ is defined as for K_D described above but with $X_{FeSiO_3}^{bm} = \frac{Fe^{3+} + Fe^{2+}}{Fe^{3+} + Fe^{2+} + Mg}$.

5

The modelled $K_{D(app)}$ values show a pressure trend in agreement with experimental data obtained on a pyrolite bulk composition[7] (Extended Data Fig. 5). (4) For the model that invokes disproportionation of FeO, an additional constraint is employed: the oxygen content of the lower mantle was fixed to the value expected for the upper mantle, that is, $Fe^{3+}/\Sigma Fe = 0.03$ (ref. 47) by including oxygen in the mass balance. It is assumed that the increased $Fe^{3+}/\Sigma Fe$ ratio in bridgmanite is balanced by the presence of metallic iron through the disproportionation reaction $3FeO = Fe_2O_3 + Fe$. The proportion of Fe metal is constrained through the oxygen mass balance.

Modelling of seismic velocities. We used the thermodynamic formalism of ref. 44 to calculate seismic wave velocities at pressure and temperature conditions of the lower mantle from our measurements at room temperature. The employed parameters are summarized in Extended Data Table 3. We included new parameters for the $FeAlO_3$ component that are chosen to provide the best fit to our measurements on $(Mg_{0.9}Fe_{0.1}Si_{0.9}Al_{0.1})O_3$. We also modified the parameters for FeO to match data previously measured using single-crystal Brillouin scattering on $(Mg_{0.9}Fe_{0.1})O$ (Extended Data Figs 3, 4). The chemical compositions of the measured samples are very close to those expected in pyrolite and extrapolations in chemical compositions are small. The thermal parameters are well constrained by previous experiments[2,4]. We note that changing the thermal parameter η that corrects the shear modulus for temperature effects by 10% (to account for different results from recent experiments[2,4] and computations[30]) does not compensate the difference in velocity gradients of our model compared to PREM. We calculate a model geotherm from the same thermodynamic parameters assuming a temperature of 1,873 K at the top of lower mantle. In the depth region modelled in our paper, the calculated temperature profile is very similar to previous work[48] (deviation is <25 K at 1,200 km depth).

Data availability. All data relevant to the conclusions of the paper are summarized in Extended Data Tables 1 and 3 and in the Source Data for Fig. 3. Further data are available from the authors on request.

34. Marquardt, H., Speziale, S., Koch-Müller, M., Marquardt, K. & Capitani, G. C. Structural insights and elasticity of single-crystal antigorite from high-pressure Raman and Brillouin spectroscopy measured in the (010) plane. *Am. Mineral.* **100,** 1932–1939 (2015).
35. Schulze, K., Buchen, J., Marquardt, K. & Marquardt, H. Multi-sample loading technique for comparative physical property measurements in the diamond-anvil cell. *High Press. Res.* (in the press).
36. Kantor, I. *et al.* BX90: A new diamond anvil cell design for X-ray diffraction and optical measurements. *Rev. Sci. Instrum.* **83,** 125102 (2012).
37. Kurnosov, A. *et al.* A novel gas-loading system for mechanically closing of various types of diamond anvil cells. *Rev. Sci. Instrum.* **79,** 045110 (2008).
38. Whitfield, C. H., Brody, E. M. & Bassett, W. A. Elastic moduli of NaCl by Brillouin scattering at high pressure in a diamond anvil cell. *Rev. Sci. Instrum.* **47,** 942–947 (1976).
39. Sinogeikin, S. V. & Bass, J. D. Single-crystal elasticity of pyrope and MgO to 20 GPa by Brillouin scattering in the diamond cell. *Phys. Earth Planet. Inter.* **120,** 43–62 (2000).
40. Speziale, S., Marquardt, H. & Duffy, T. S. in *Spectroscopic Methods in Mineralogy and Materials Science,* Vol. 78, 543–603 (Mineral Society of America, 2014).
41. Trots, D. *et al.* Elasticity and equation of state of $Li_2B_4O_7$. *Phys. Chem. Miner.* **38,** 561–567 (2011).
42. Angel, R. & Finger, L. W. SINGLE: a program to control single-crystal diffractometers. *J. Appl. Cryst.* **44,** 247–251 (2011).
43. Pamato, M. G. *et al.* Single-crystal elasticity of majoritic garnets: stagnant slabs and thermal anomalies at the base of the transition zone. *Earth Planet. Sci. Lett.* **451,** 114–124 (2016).
44. Stixrude, L. & Lithgow-Bertelloni, C. Thermodynamics of mantle minerals – I. Physical properties. *Geophys. J. Int.* **162,** 610–632 (2005).
45. McDonough, W. F. & Sun, S.-S. Composition of the Earth. *Chem. Geol.* **120,** 223–253 (1995).
46. Stixrude, L. & Lithgow-Bertelloni, C. Thermodynamics of mantle minerals – II. Phase equilibria. *Geophys. J. Int.* **184,** 1180–1213 (2011).
47. Canil, D. & O'Neill, H. S. C. Distribution of ferric iron in some upper-mantle assemblages. *J. Petrol.* **37,** 609–635 (1996).
48. Brown, J. M. & Shankland, T. J. Thermodynamic parameters in the Earth as determined from seismic profiles. *Geophys. J. R. Astron. Soc.* **66,** 579–596 (1981).
49. Lin, J. F. *et al.* Sound velocities of hot dense iron; Birch's law revisited. *Science* **308,** 1892–1894 (2005).
50. Tange, Y., Takahashi, E., Nishihara, Y., Funakoshi, K.-i. & Sata, N. Phase relations in the system MgO-FeO-SiO_2 to 50 GPa and 2000°C: an application of experimental techniques using multianvil apparatus with sintered diamond anvils. *J. Geophys. Res.* **114,** B02214 (2009).
51. Wolf, A. S., Jackson, J. M., Dera, P. & Prakapenka, V. B. The thermal equation of state of (Mg, Fe)SiO_3 bridgmanite (perovskite) and implications for lower mantle structures. *J. Geophys. Res.* **120,** 7460–7489 (2015).
52. Speziale, S., Zha, C. S., Duffy, T. S., Hemley, R. J. & Mao, H. K. Quasi-hydrostatic compression of magnesium oxide to 52 GPa; implication for the pressure-volume-temperature equation of state. *J. Geophys. Res. B* **106,** 515–528 (2001).
53. Fischer, R. A. *et al.* Equation of state and phase diagram of FeO. *Earth Planet. Sci. Lett.* **304,** 496–502 (2011).
54. Xu, W., Lithgow-Bertelloni, C., Stixrude, L. & Ritsema, J. The effect of bulk composition and temperature on mantle seismic structure. *Earth Planet. Sci. Lett.* **275,** 70–79 (2008).
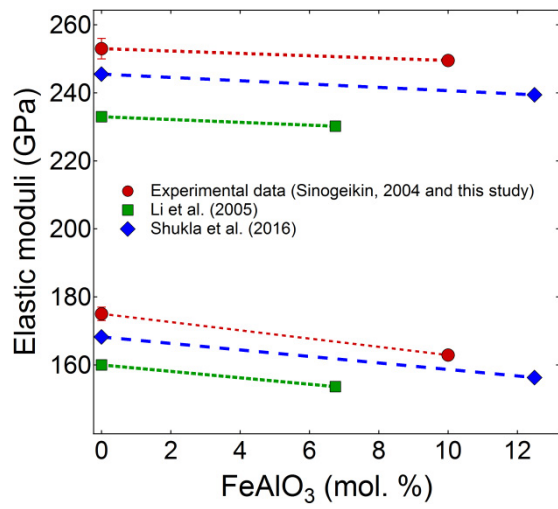
Extended Data Figure 1 | Effect of FeAlO$_3$ incorporation on the room pressure elastic moduli of MgSiO$_3$ bridgmanite. The red circles represent data based on this study on (Al,Fe)-bearing bridgmanite and earlier Brillouin scattering work on single-crystal MgSiO$_3$ bridgmanite[13]. The blue and green symbols refer to computational studies[14,18].
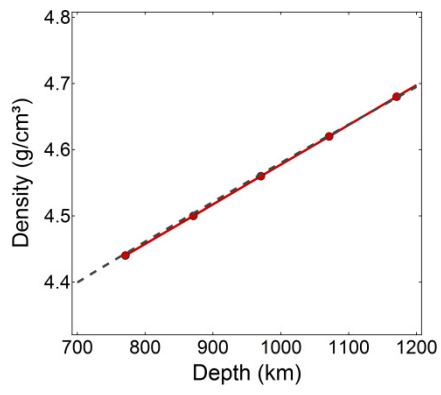
Extended Data Figure 2 | Densities (red curve) as a function of depth calculated from our model. The dashed line corresponds to PREM.
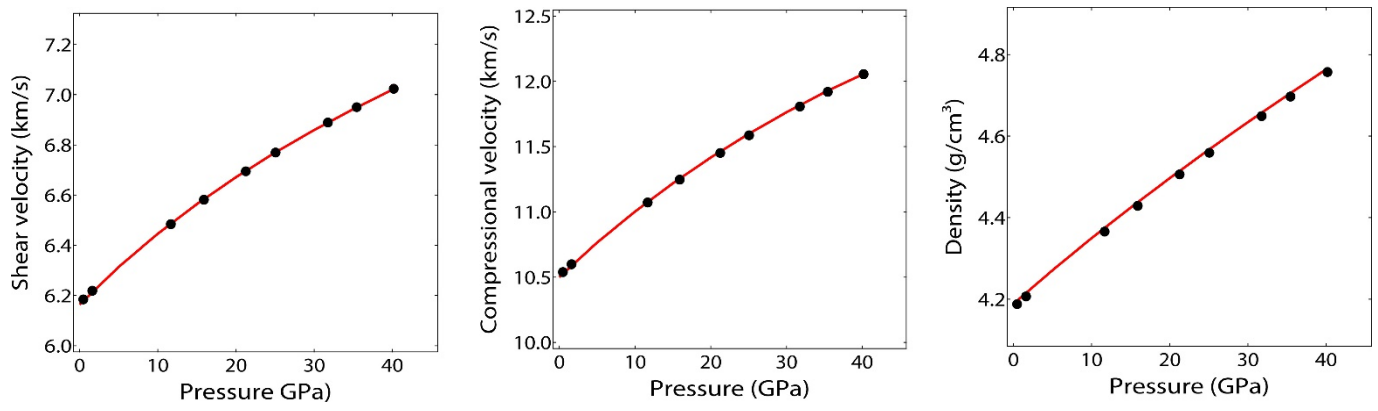
Extended Data Figure 3 | Modelled sound wave velocities for $(Mg_{0.9}Fe_{0.1}Si_{0.9}Al_{0.1})O_3$ (red curves) along with the experimental data from this study.
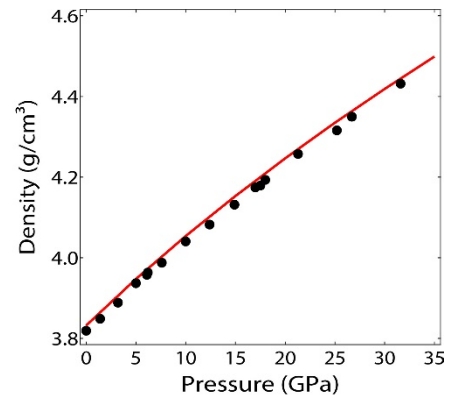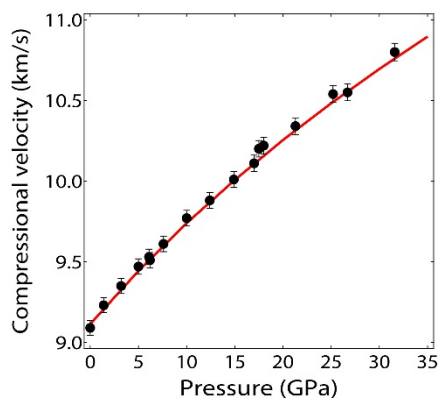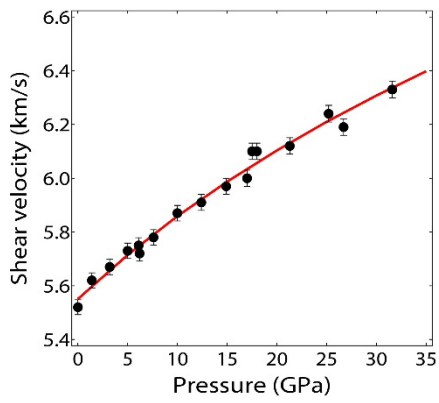
Extended Data Figure 4 | Modelled sound wave velocities. For $(Mg_{0.9}Fe_{0.1})O$ (red curves) along with experimental data[29]. The data below 35 GPa have been employed to constrain the physical properties of the FeO and MgO components in the model as the effects of the iron spin transition are not captured by the model. At the temperature conditions of Earth's mantle, the effects of the iron spin crossover will be shifted to depths beyond those modelled in this study[21] and are, therefore, irrelevant to the present contribution.
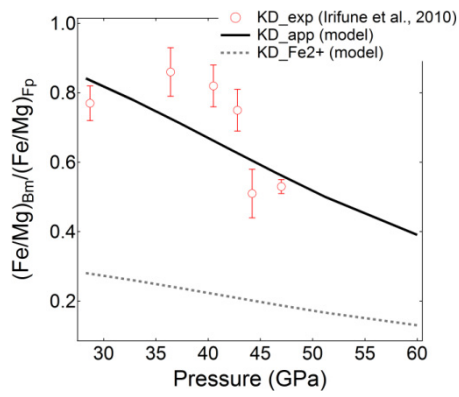
Extended Data Figure 5 | Fe-partitioning coefficient $K_{D(app)}$ from our model in comparison to previous experimental data measured on a pyrolitic mantle composition. The thermodynamic model not only matches available elasticity data for bridgmanite and ferropericlase (Extended Data Figs 3, 4) but also reproduces changes in Fe–Mg partitioning between these phases with depth in both Al-free and Al-bearing systems.
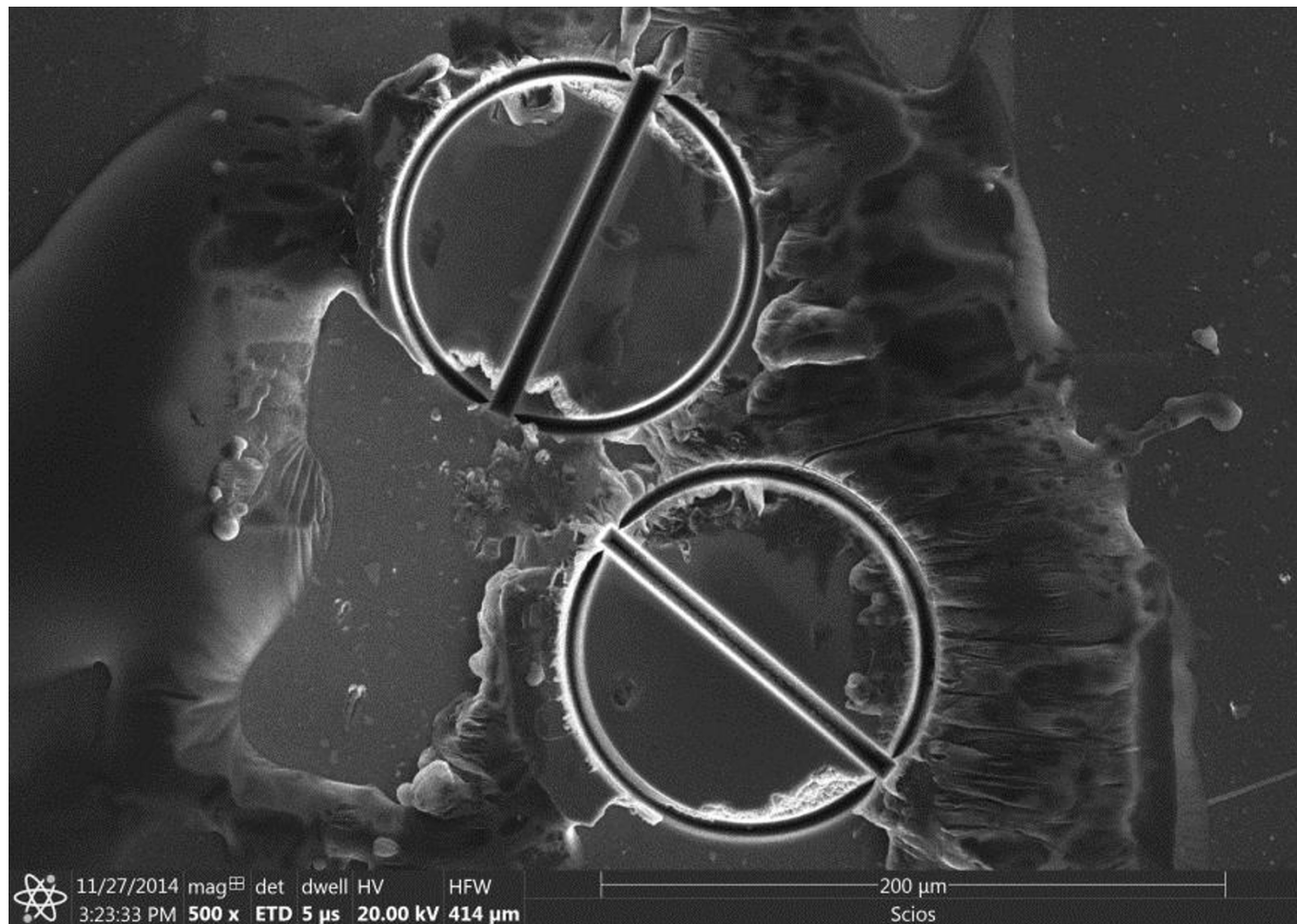
Extended Data Figure 6 | Secondary electron image of polished single crystals of bridgmanite. Crystals have been cut to half-circles by a focused ion beam[12,34].
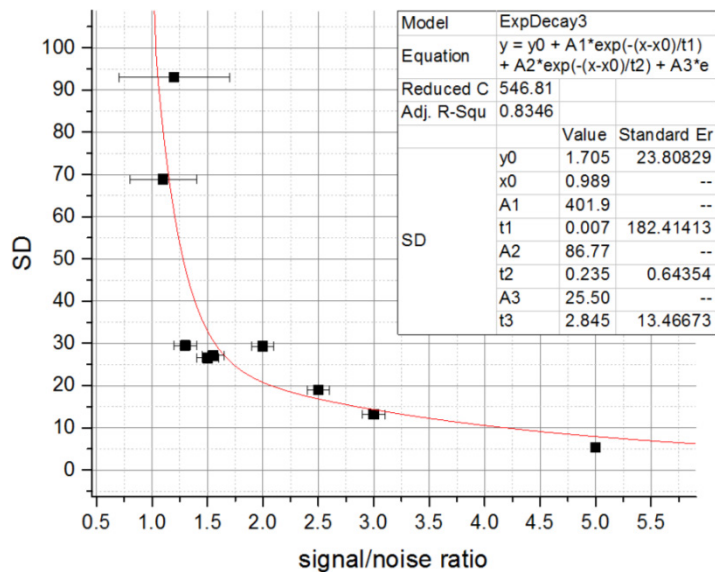
Extended Data Figure 7 | Standard deviation as a function of the signal-to-noise ratio in Brillouin spectra.

Extended Data Table 1 | Summary of high-pressure elastic constants derived for (Mg$_{0.9}$Fe$_{0.1}$Si$_{0.9}$Al$_{0.1}$)O$_3$

P (GPa)	rho (g/cm³)	C$_{11}$ (GPa)	C$_{22}$ (GPa)	C$_{33}$ (GPa)	C$_{44}$ (GPa)
0.48	4.188	463.3(14)	512.6(21)	429.1(4)	189.7(5)
1.62	4.207	467.8(14)	520.9(20)	437.3(4)	191.8(5)
11.68	4.366	505.9(15)	593.1(20)	508.6(4)	210.2(4)
15.93	4.429	520.9(18)	622.9(25)	538.2(5)	217.6(3)
21.32	4.506	539.0(22)	660.3(33)	575.5(7)	226.7(3)
25.16	4.559	551.4(26)	686.6(40)	601.9(8)	233.0(3)
31.92	4.649	572.2(34)	732.4(52)	648.0(11)	243.8(3)
35.66	4.697	583.1(39)	757.4(60)	673.3(13)	249.6(4)
40.44	4.757	596.6(45)	789.2(70)	705.5(15)	256.8(4)

P (GPa)	C$_{55}$ (GPa)	C$_{66}$ (GPa)	C$_{12}$ (GPa)	C$_{13}$ (GPa)	C$_{23}$ (GPa)
0.48	167.4(3)	128.6(14)	142.8(11)	131.0(8)	162.4(10)
1.62	169.2(3)	132.3(14)	145.0(11)	133.7(8)	165.6(9)
11.68	183.6(2)	165.3(11)	163.9(10)	156.7(8)	193.7(10)
15.93	189.3(2)	179.3(11)	171.6(11)	166.3(9)	205.4(12)
21.32	196.3(2)	197.1(12)	181.3(14)	178.4(12)	220.2(15)
25.16	201.1(2)	209.8(14)	188.0(16)	187.0(14)	230.7(18)
31.92	209.2(3)	232.3(17)	199.7(21)	202.0(19)	249.1(23)
35.66	213.4(3)	244.8(19)	206.1(24)	210.2(22)	259.2(27)
40.44	218.8(3)	260.8(22)	214.2(28)	220.7(25)	272.1(31)

Numbers in parentheses refer to a 1σ uncertainty in the last reported digit.

Extended Data Table 2 | Summary of ambient pressure elastic constants reported for MgSiO$_3$ and (Fe,Al)-bearing MgSiO$_3$ from both experimental and theoretical work

Mol.% FeAlO$_3$	C$_{11}$ (GPa)	C$_{22}$ (GPa)	C$_{33}$ (GPa)	C$_{44}$ (GPa)	C$_{55}$ (GPa)	C$_{66}$ (GPa)	C$_{12}$ (GPa)	C$_{13}$ (GPa)	C$_{23}$ (GPa)	Method	Ref.
0	482(4)	537(3)	485(5)	204(2)	186(2)	147(3)	144(6)	147(6)	146(7)	Experiment	15
0	481(4)	528(3)	456(4)	200(2)	182(2)	147(2)	125(3)	139(3)	146(3)	Experiment	13
0	438	488	422	182	163	134	118	122	136	Theory	14
6.75	428.4	476.8	409.6	174.2	157.6	129.4	119.6	124	137	Theory	14
10	461.3 (17)	509.7 (26)	425.7 (5)	188.8 (6)	166.5 (4)	127.2 (17)	141.7 (14)	130.0 (11)	161.0 (12)	Experiment	This study

The constants from the computational work are reported at -7 GPa as a result of an applied pressure correction[14].

Extended Data Table 3 | Summary of parameters used for the model calculations

Phase	Component	F_0 (kJ/mol)	V_0 (cm³/mol)	K_0 (GPa)	K'_0	Θ_0 (K)	γ_0	q	G_0 (GPa)	G'_0	η
Fe	Fe		6.73	164	4	422	1.71	1.4	81.5	1.9	7
Bm	$MgSiO_3$	-136.8	24.45	251	4.1	905	1.57	1.1	173	1.7	2.3[1]
	$FeSiO_3$	-104.3[2]	25.34[3]	272	4.1	871	1.57	0.6[4]	133	1.4	2.3
	$FeAlO_3$		**26.9**	**220**	**1.3**	886	1.57	1.1	**96**	**3.4**	2.5
	$AlAlO_3$		24.94	258	4.1	886	1.57	1.1	171	1.5	2.5
Fp	MgO	-569	11.24	160.2[5]	3.99[5]	767	1.36	1.7	131	2.1	2.8
	FeO	-242	12.26	149[6]	3.6[6]	454	1.53	1.7	60[7]	1.8[7]	0.6[8]
Ca-Pv	$CaSiO_3$		27.54	236	3.9	802	1.89	0.9	157	2.2	1.3

Non-bold values without superscript numbers are taken from ref. 46. Bold numbers are based on this study. The parameters for the (fictive) $FeAlO_3$ have been derived from those obtained in this study for the (Fe,Al)-bearing bridgmanite for the purpose of the thermodynamic modelling of seismic wave velocities in the lower mantle. These endmember values are used only in the computation of the properties for bridgmanites involving dilute solutions of the $FeAlO_3$ component as those present in the studied sample. Some of the $FeSiO_3$ parameters have been updated in agreement with recent findings in order to provide the best fit of K_D values, which are sensitive to the equation of state parameters of the $FeSiO_3$ component. We note that the seismic model is almost insensitive to these parameters. The parameters for Fe were extracted from a previous study[49]. Superscripts: (1) value lies in between recently reported values[2,30,46]; (2) value has been chosen to provide the best fit to experimentally determined partitioning coefficients reported in ref. 7; (3) based on ref. 50; (4) based on ref. 51; (5) from ref. 52; (6) from ref. 53; (7) based on data from ref. 29; (8) from ref. 54.

CORRECTIONS & AMENDMENTS

Author Correction: Evidence for a Fe^{3+}–rich pyrolitic lower mantle from (Al,Fe)–bearing bridgmanite elasticity data

A. Kurnosov, H. Marquardt, D. J. Frost, T. Boffa Ballaran & L. Ziberna

In Extended Data Table 1 of this Letter, some of the elastic constants were reported incorrectly. This occurred as a result of an error in the script used to generate the numbers. The values of the elastic constants at room pressure cited in the manuscript on page 544 were derived using the same erroneous script, and the correct values and 1σ-uncertainties in the last given digit are $C_{11} = 461.3(17)$ GPa instead of 462.7(17) GPa; $C_{22} = 509.7(26)$ GPa instead of 504.9(26) GPa; $C_{33} = 425.7(5)$ GPa instead of 426.6(5) GPa; $C_{44} = 188.8(6)$ GPa instead of 188.4(6) GPa; $C_{55} = 166.5(4)$ GPa instead of 166.6(4) GPa; $C_{66} = 127.2(17)$ GPa instead of 129.7(17) GPa; $C_{12} = 141.7(14)$ GPa instead of 140.2(14) GPa; $C_{13} = 130.0(11)$ GPa instead of 132.2(11) GPa; and $C_{23} = 161.0(12)$ GPa instead of 159.3(12) GPa. These errors do not affect any of the conclusions and we apologize for any confusion this may have caused. Extended Data Table 1 and the room-pressure values in the text have been corrected online. The Supplementary Information of this Amendment contains the original, incorrect Extended Data Table 1, for transparency.

Supplementary Information is available in the online version of this Amendment.